



## Article

# Landslide Hazard Assessment for Wanzhou Considering the Correlation of Rainfall and Surface Deformation

Xiangjie She, Deying Li \*, Shuo Yang, Xiaoxu Xie, Yiqing Sun and Wenjie Zhao

Faculty of Engineering, China University of Geosciences, Wuhan 430074, China; shexiangjie@cug.edu.cn (X.S.); yang\_shuo@cug.edu.cn (S.Y.); xiexx@cug.edu.cn (X.X.); syiqing@cug.edu.cn (Y.S.); zhaowenjie@cug.edu.cn (W.Z.)  
\* Correspondence: lideying@cug.edu.cn

**Abstract:** The landslide hazard assessment plays a crucial role in landslide risk mitigation and land use planning. The result of landslide hazard assessment corrected by surface deformation, obtained through time-series InSAR, has usually proven to have good application capabilities. However, the issue lies in the uncertainty of InSAR results, where some deformations cannot be calculated, and some are not true deformations. This uncertainty of InSAR results will lead to errors in landslide hazard assessment. Here, we attempt to evaluate landslide hazards by considering combined rainfall and surface deformation. The main objective of this research was to mitigate the impact of bias and explore the accurate landslide hazard assessment method. A total of 201 landslides and 11 geo-environment factors were utilized for landslide susceptibility assessment by support vector machine (SVM) model in Wanzhou District, Three Gorges Reservoir Area (TGRA). The preliminary hazard is obtained by analyzing the statistical data of landslides and rainfall. Based on the SAR image data of Sentinel-1A satellites from September 2019 to October 2021, the SBAS-InSAR method was used to analyze surface deformation. The correlation between surface deformation and rainfall was analyzed, and the deformation factor variables were applied to landslide hazard assessment. The research results demonstrate that the error caused by the uncertainty of InSAR results can be effectively avoided by analyzing the relationship between rainfall and surface deformation. Our results can effectively adjust and correct the hazard results and eliminate the errors in the general hazard assessment. Our proposed method can be used to assess the landslide hazard in more detail and provide a reference for fine risk management and control.



**Citation:** She, X.; Li, D.; Yang, S.; Xie, X.; Sun, Y.; Zhao, W. Landslide Hazard Assessment for Wanzhou Considering the Correlation of Rainfall and Surface Deformation. *Remote Sens.* **2024**, *16*, 1587. <https://doi.org/10.3390/rs16091587>

Academic Editor: Sandro Moretti

Received: 13 March 2024

Revised: 14 April 2024

Accepted: 21 April 2024

Published: 29 April 2024



**Copyright:** © 2024 by the authors. Licensee MDPI, Basel, Switzerland. This article is an open access article distributed under the terms and conditions of the Creative Commons Attribution (CC BY) license (<https://creativecommons.org/licenses/by/4.0/>).

**Keywords:** landslide hazard assessment; SBAS InSAR; correlation; deformation factor; Three Gorges Reservoir Area

## 1. Introduction

Landslide disasters are common geological disasters, occurring widely in strong earthquake areas, reservoir areas and mountainous areas [1–4]. Due to the suddenness, concealment and frequency characteristics, the infrastructure and live of the residents are seriously threatened by landslides. Therefore, landslide hazard evaluation plays an important role in land use planning, engineering site selection, and landslide risk mitigation [5,6].

Landslide hazard assessment is a critical part of risk assessment, aiming to evaluate the spatial and temporal probability of landslide occurrence. Generally, the spatial probability of landslide occurrence is delineated by the susceptibility assessment based on the historical and present landslide events, and the temporal probability is analyzed by a physical model or statistical model of previous landslides [7,8]. However, for the large study area, landslide hazard is affected by geo-environment, rainfall, human activities, etc., which means that the precision of the physical model is limited by the parameter uncertainty [9–11]. Therefore, statistical analysis has wider application scenarios. In recent years, the difference and dynamic change in landslide hazard at different periods was noticed by researchers. For instance, the influence of rainfall intensities and meteorological conditions in landslide hazard

assessment was studied [12,13]. With the development and maturity of InSAR technology, it has been widely used in the study of monitoring and landslide identification [14–20]. The surface deformation based on InSAR has also been introduced into dynamic landslide hazard assessment [14–16].

The surface deformation of the landslide at a certain time period can reflect the current situation of the landslide hazard. As is well known, time-series InSAR technology has the characteristics of wide coverage, high precision and short periods [17–20]. Therefore, the surface deformation data obtained from time-series InSAR are not only useful for landslide monitoring and identification [21–24] suit for dynamic landslide hazard assessment [25–28]. Yi Zhang et al. used the information on surface deformation extracted by SBAS-InSAR as an internal index to establish a machine-learning model for landslide hazard analysis [16]. Guo Zhang et al. used the WOE model and static factor data for the LS map. They used the contribution matrix to grade and assign values to susceptibility and surface deformation and produced a more accurate and reasonable LS distribution [25]. Yunfeng Shan et al. propose a novel method for assessing landslide hazards by combining deformation results from ascending and descending SAR data images. They constructed hazard matrices for all InSAR surface deformation results for different orbits, thus carrying out a more temporal hazard evaluation [26]. Chao Zhou et al. considered the seasonality of rainfall in the Three Gorges Reservoir Area, used the ground deformation velocity extracted from MT-InSAR, and used an empirical matrix to evaluate the dynamic landslide hazard in two periods of a water year [27]. It demonstrates that it is achievable to incorporate time-series InSAR into the landslide hazard assessment for long-term sustainable assessment and dynamic adjustment.

However, the surface deformation obtained by InSAR technology is uncertain, some of them cannot be calculated, and some are not real landslide deformations. It means that the landslide hazard assessment result will be induced bias by the direct introduction of surface deformation obtained from InSAR. For instance, the surface deformation is only used as an intrinsic index to be added directly into the evaluation model [16] or simply superimposed with other evaluation indicators (spatial probability, rainfall) [25–29]. Especially in the hazard assessment of rainfall-induced landslides, most landslide surface deformations are caused by rainfall. The current research severed the relationship between surface deformation and rainfall events. No attention was paid to the correspondence between surface deformation and rainfall events, which resulted in some errors in the evaluation results. This type of deformation should be effectually introduced in dynamic and precise hazard evaluations rather than ignore the relationship between surface deformation and rainfall events.

Therefore, the intent of this paper is to alleviate the bias caused by directly introducing surface deformation obtained by InSAR in landslide risk assessment by analyzing the correlation between rainfall and surface deformation. The Wanzhou District of the Three Gorges Reservoir Area was selected as the study area. The preliminary landslide hazard assessment result was constructed by the spatial probability (analyzed by landslide susceptibility) and the temporal probability (obtained by rainfall events). The surface deformation from 2019 to 2021 was extracted by PS+SBAS InSAR, and the correlation between surface deformation and rainfall was analyzed. The deformation factor was applied to the preliminary assessment results. Through this assessment framework, more accurate and more practical dynamic assessment results of landslide hazards were provided.

## 2. Study Area

The study area in Wanzhou is located in the northeastern part of Chongqing, China. The area belongs to the Three Gorges Reservoir Area (TGRA), and the Yangtze River passes through the area from southwest to northeast (Figure 1). It is located in a humid subtropical monsoon climate area with abundant rainfall. The average annual rainfall is 1200 mm, and the maximum annual rainfall is 1641 mm. The maximum monthly rainfall is 683 mm. The rainy season is from April to October, and the cumulative rainfall accounts for about 80–90% of the total annual rainfall. The water level in the Yangtze River has been raised

from the original level to 175 m since 2003 due to the construction of the Three Gorges Dam. The reservoir water level fluctuates from 145 m to 175 m every year. The big rise and periodic fluctuations in reservoir water level significantly change the local groundwater flow in the reservoir banks, which often results in landslide occurrence. The landslides in the reservoir banks are influenced by reservoir water level and/or heavy rainfall.

The geology is an important factor affecting landslide occurrence and evolution. It is located on the eastern edge of the Sichuan Basin, where the geological structure is complex with dense fold structure. However, there is no large-scale fracture tectonic movement. The Jurassic and Triassic sedimentary rocks are widely distributed in the area overlain by Quaternary soils, mainly including sandstones and mudstones. The landslides often occur in the mudstone layers, where the soft rocks are easily transferred to soil in heavy rainfall and reservoir water levels. The area is located in a high landslide susceptibility zone. The inventory of 201 landslides in the area was obtained from remote sensing, field investigations and landslide reports, as shown in Figure 1. Detailed landslide records span a period of 20 years from 1997 to 2017, including landslide type, failure time, location, landslide process, loss, etc. The landslides are mainly distributed in the reservoir banks and most of them are colluvial landslides triggered by rainfall and reservoir water level.

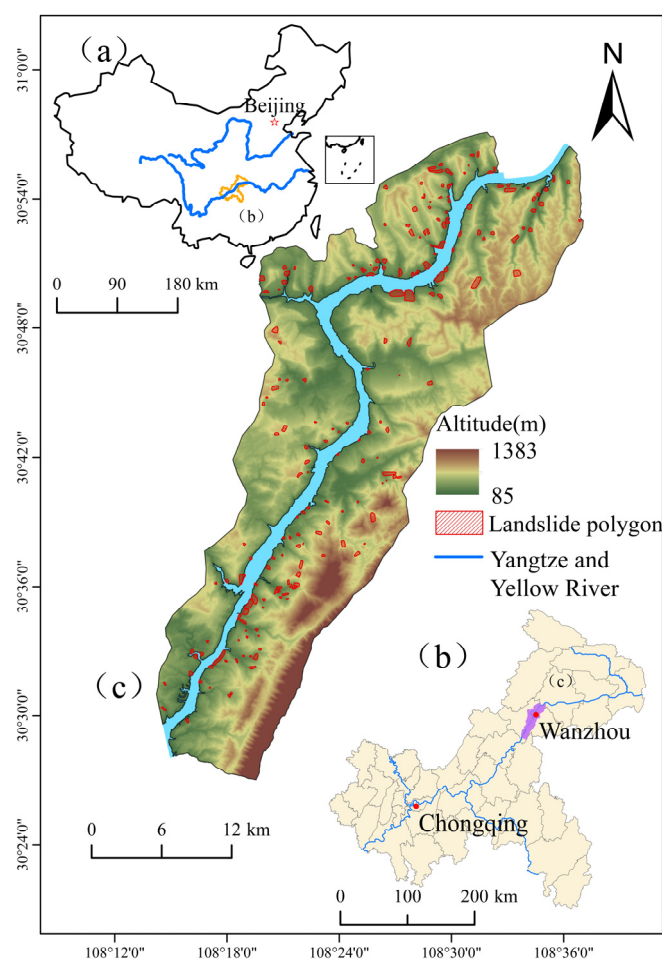


**Figure 1.** (a) Geographic location of the study area. (b) Chongqing, China; (c) landslides map in the study area.

### 3. Methods

Rainfall is the main trigger of landslide deformation and landslide failure. For single landslides, the relationship between landslide deformation and rainfall was widely studied based on long-term monitoring data [30]. However, landslide deformation was seldom used for regional landslide hazard assessment. In the paper, the regional landslide defor-

mation obtained from the time-series InSAR method was attempted for landslide hazard analysis. The preliminary landslide hazard assessment considering rainfall trigger factors was first obtained by probabilistic analysis. The final result of the landslide hazard assessment was corrected through the regional landslide surface deformation. The flowchart of landslide hazard assessment is shown in Figure 2. It is mainly divided into four steps: (1) Landslide inventory in the study area was obtained by remote sensing interpretation, field investigation and data collection. The predisposing factors of landslides were determined. The machine learning method (SVM) was adopted to predict the regional landslide susceptibility. (2) The historical rainfall data and landslide records were collected to analyze the temporal probability of landslide occurrence under different rainfall intensities. The preliminary result of landslide hazard evaluation was gained through the combination with the landslide susceptibility result. (3) The Sentinel-1 provides free SAR images for regional image interpretation. The integrated PS+SBAS time-series InSAR method was used to research the surface deformation. The correlation between surface deformation and rainfall was analyzed to provide an effective deformation factor. (4) The empirical matrix considering surface deformation and the preliminary landslide hazard result was constructed to get the final landslide hazard assessment result. In the study, the key is to find out the relationship between surface deformation and rainfall in a certain period and apply it to the landslide hazard assessment.

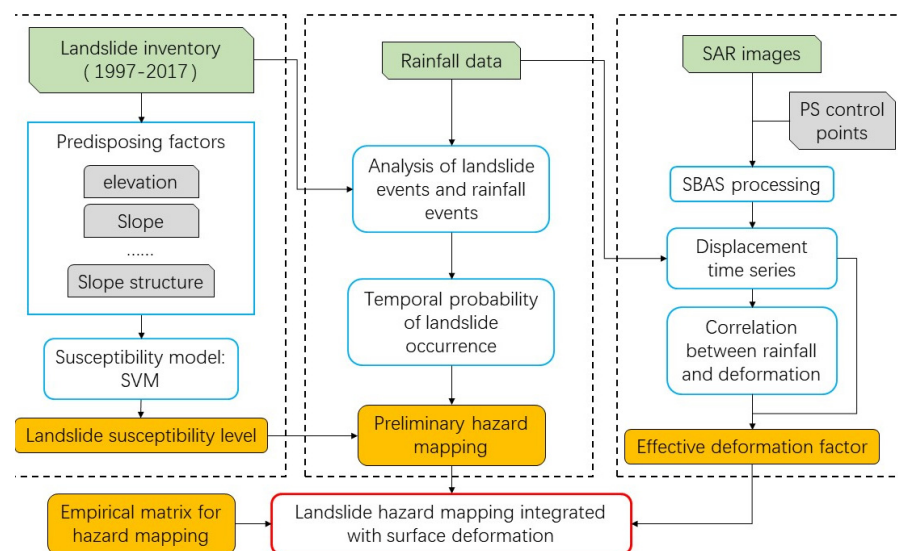


**Figure 2.** Flowchart of landslide hazard assessment considering surface deformation.

### 3.1. Landslide Susceptibility Assessment

Landslide susceptibility assessment is the quantification of the spatial probability of landslide occurrence. The basic assumption of landslide susceptibility assessment is that “Future landslide events are more likely to occur under conditions similar to those of previous landslide events” [31]. Therefore, the landslide possibility of the study area was predicted by analyzing the environmental conditions where the landslide events had occurred. Statistical methods and machine learning models are often used in the landslide susceptibility assessment, which are data-driven methods. Among them, support vector machine (SVM) has been widely used in landslide susceptibility evaluation due to its excellent classification ability [27,32,33].

In this paper, the support vector machine was adopted to evaluate the landslide susceptibility. Through the analysis of landslide occurrence and landslide triggers, the 14 variables were extracted from DEM and geology map as landslide susceptibility evaluation factors (Figure 3), including elevation, slope, aspect, topographic wetness index (TWI), topographic roughness index (TRI), distance from gullies, distance from roads, topographic curvature, plane curvature, land use, distance from rivers, slope structure, lithology and

normalized difference vegetation index (NDVI). After multiple covariance analyses and importance calculations, 11 evaluation factors are finally selected, as shown in Table 1. In the study, landslide data and evaluation factors have been rasterized and resampled to 20 m × 20 m pixel grid units. A total of 70% of the known landslides were used for training, and the remaining 30% was for validation. Finally, the ROC index was used to evaluate the landslide susceptibility result.

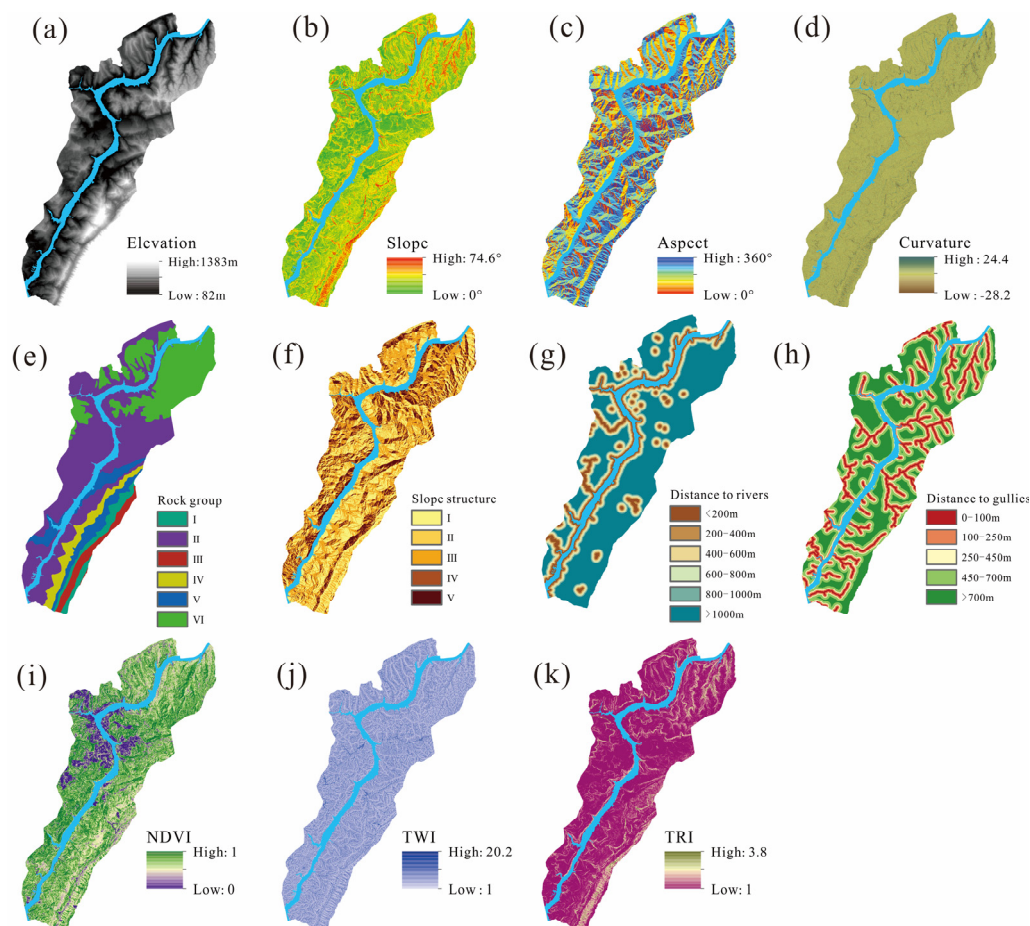


**Figure 3.** Landslide susceptibility assessment factors. (a) Elevation; (b) slope; (c) aspect; (d) curvature; (e) engineering geological rock group; (f) slope structure; (g) distance to rivers; (h) distance to gullies; (i) NDVI; (j) TWI; (k) TRI.

**Table 1.** Predictor factors.

Factors	Class
Elevation	137–350 m, 350–550 m, 550–780 m, 780–1141 m
Slope	0–5°, 5–15°, 15–30°, 30–45°, >45°
Aspect	0–45°, 45–90°, 90–135°, 135–180°, 180–225°, 225–270°, 270–315°, 315–360°
Curvature	<–2, –2–0, 0–3, >3
Engineering geological rock group	I (hard thick limestone rock group), II (hard thick sandstone intercalated with shale rock group), III (hard middle argillaceous limestone rock group), IV (soft thin mudstone shale rock group), V (hard thick lithic sandstone rock group), VI (harder middle sandstone rock group)

Table 1. Cont.

Factors	Class
Slope structure	I: dip slope, II: dip-diagonal slope, III: transverse slope, IV: reverse-diagonal slope, V: reverse slope
Topographic wetness index (TWI)	<5.9, 5.9–8.3, 8.3–12, >12
Topographic roughness index (TRI)	1–1.2, 1.2–1.4, 1.4–3.7
Normalized difference vegetation index (NDVI)	Bare land (0–0.3), low vegetation cover (0.3–0.5), medium vegetation coverage (0.5–0.7), high coverage vegetation (0.7–1.0)
Distance to rivers	<200 m, 200–400 m, 400–600 m, 600–800 m, 800–1000 m, >1000 m
Distance to gullies	0–100 m, 100–250 m, 250–450 m, 450–700 m, >700 m

### 3.2. Landslide Hazard Analysis Based on Rainfall

Landslide hazard assessment (LHA) aims to determine the spatial-temporal probability of landslide occurrence in the target area within a specified period of time. The frequency or return period of landslide events under specific triggering conditions of rainfall or earthquake was considered in the common practice [27,34,35]. The landslide hazard index  $H$  in relation to the triggering factor of rainfall can be expressed as follows:

$$H = P(s) \times P(t) \times P(e) \quad (1)$$

where  $P(s)$  is the spatial probability of landslide occurrence, also known as the landslide susceptibility index;  $P(t)$  is the temporal probability of a specific triggering event. When a specific triggering event was considered to have occurred,  $P(t)$  was equal to 1;  $P(e)$  is the probability of landslide failure in response to the triggering event.

In this study, 201 landslides in the area that had occurred from 1997 to 2017 are selected as samples. Among them, there were 159 rainfall-induced landslides and 41 landslides induced by a combination of rainfall, reservoir levels or human engineering activities. Therefore, rainfall was the main trigger for the landslides in the area. The landslide hazard assessment was conducted by considering rainfall as a landslide-inducing event. The daily rainfall records from 1997 to 2017 in the area were collected in the landslide inventory. The occurrence of landslide events is not only related to the rainfall on the current day of landslide occurrence but also influenced by the previous cumulative rainfall [36]. Liu (2014) had already demonstrated that the landslide event in Wanzhou was mostly correlated with the antecedent 5-day total rainfall [37]. Therefore, when comparing the probability of rainfall events with the probability of landslide occurrence, we use it to represent rainfall intensity.

### 3.3. Time-Series InSAR

The time-series InSAR is a more prevalent approach for measuring surface deformation and monitoring due to the capture of a broad spectrum of deformation with high precision [38–40]. The permanent scatterer interferometry (PS-InSAR) technique was proposed by Ferretti and colleagues [41]. This method often chooses one image as the primary one and the others as secondary ones from a series of multiple images over the same area. Stable and permanent scattering points were achieved by registering and interfering with both the primary and secondary images because ground objects can maintain strong, stable electromagnetic scattering properties over a long time. The phase of surface deformation is determined by analyzing the phase information of the permanent scattering points and removing the noise phase. Small Baseline Subset-Interferometric Synthetic Aperture Radar (SBAS-InSAR) is a time-series analysis method based on the nature of distributed scatterers proposed by Berardino et al. [42] It can reduce the de-correlation induced by long spatial or temporal baselines and mitigate the effects of atmospheric effects and terrain errors. The time-series ground deformation is achieved through the least squares method and the singular value decomposition method (SVD) to guarantee millimeter-level accuracy.

Both PS-InSAR and SBAS-InSAR methods have demonstrated excellent behavior in obtaining landslide surface deformation. However, due to the complex terrain, dense gullies, large fluctuations in elevation and lush vegetation, both traditional analytical methods have their limitations in high mountainous areas [43]. PS technology can generate ground control points with high coherence and it is mainly applied for obtaining linear deformation. Although SBAS technology has some subjectivity in selecting ground control points, it performs well in analyzing distributed targets. In order to develop the advantages of PS-InSAR and SBAS-InSAR, the two time-series InSAR methods were both used to obtain surface deformation in the study area. The SBAS-InSAR technology was used in the data processing. In order to enhance the accuracy of SBAS-InSAR processing, the high-coherence ground control points were obtained through PS-InSAR technology in the orbit refinement, which can eliminate residual phase information.

The Sentinel-1A satellite image data, Digital Elevation Model (DEM) and precise orbit data of Sentinel satellites were used in the analysis of time-series InSAR. The Sentinel-1 mission consists of two near-polar orbiting satellites with C-band synthetic aperture radar sensors, launched by the European Space Agency in 2014. Each satellite has a revisit time of 12 days. A total of 57 ascending orbit images of Sentinel-1A from September 2019 to October 2021 were collected for the time-series InSAR analysis to calculate the deformation results of the LOS direction (VSLOPE) in the study area.

### 3.4. Correlation Analysis between Rainfall and Surface Deformation

In the study area, rainfall was considered the main factor leading to landslide deformation and failure [44]. For rainfall-induced landslides, there is a certain correlation between rainfall and landslide surface deformation. The correlation analysis between two variables can be conducted by an analytical method. Pearson's correlation coefficient method is a quantitative statistical approach capable of measuring the correlation between two variables in spatial data, providing sufficient interpretability [45–47]. In this study, Pearson's coefficient is used to explore the correlation between rainfall and surface deformation in the area. By statistically analyzing multiple sets of cumulative rainfall and surface deformation over the entire time period, the variables  $(X_i, Y_i)$  ( $i = 1, 2, 3, \dots, n$ ) were used to represent the two variables. The correlation coefficient can be determined using the following equation:

$$r = \frac{\sum_{i=1}^n (X_i - \bar{X})(Y_i - \bar{Y})}{\sqrt{\sum_{i=1}^n (X_i - \bar{X})^2}} \quad (2)$$

The correlation coefficient  $r$  obtained from the above formula ranges from  $-1$  to  $1$ . The closer  $|r|$  is to  $1$ , the higher the linear correlation between  $X$  and  $Y$ . If  $r = 1$ , it indicates a completely positive linear correlation between  $x$  and  $y$ . If  $r = -1$ , it indicates a completely negative linear correlation between  $x$  and  $y$ . The spatial relationship between rainfall and surface deformation in the area was represented by the correlation coefficient. A higher correlation coefficient ' $r$ ' at a specific area implies a stronger correlation between rainfall and surface deformation, which indicates that rainfall is the primary factor causing surface deformation. Conversely, a smaller ' $r$ ' value indicates a weaker correlation between surface deformation and rainfall, implying that rainfall is not the primary factor causing surface deformation.

The period of Sentinel satellite images covers from 27 September 2019 to 10 October 2021. Considering the timing and revisit period of the Sentinel satellite, the period of approximately two years was divided into 20 time units. Each time unit is 36 days, and it is three cycles of Sentinel image, as shown in Figure 4. Based on collected rainfall data and the InSAR deformation results, correlation analysis between the accumulated rainfall and surface deformation in the area within these 20 time units was conducted.

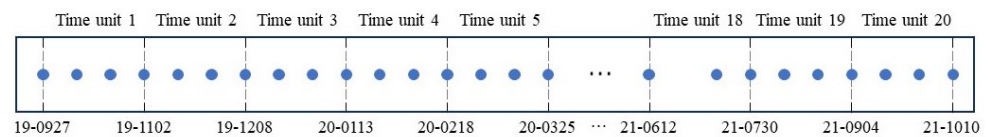


**Figure 4.** Distribution of time units and images.

### 3.5. Landslide Hazard Evaluation Considering Surface Deformation Factor

Landslide hazard assessment may become very complex due to different landslide triggers, such as rainfall, earthquakes or human activities. For example, landslide hazards may increase due to some areas undergoing surface deformation induced by human engineering activities or rainfall. Therefore, considering landslide deformation areas induced by rainfall during a specific time period becomes more precise and comprehensive in the landslide hazard assessment.

The paper explores how to combine surface deformation data and rainfall data to address such problems. Typically, in the time-series InSAR data, the positive deformation values indicate that the object is moving toward the satellite, while the negative deformation values indicate movement in the opposite direction. Researchers used positive deformation values to represent surface uplift and negative deformation values to represent subsidence. Extensive research and monitoring data demonstrated that rainfall typically promotes landslide deformation. In the source area of landslides, it generally manifests as depression and subsidence, which in InSAR deformation data appears as a movement away from the satellite, yielding negative values. Therefore, during the creeping stage of landslides, rainfall promotes downward and subsidence deformation of landslides, which in InSAR deformation data, due to its negative values, is manifested numerically as increased rainfall leading to increased subsidence, resulting in decreased InSAR deformation values, thus exhibiting a negative correlation numerically. Conversely, data that correlate positively with InSAR deformation data represent surface uplift, but in reality, there is no physical connection between surface uplift and rainfall. Therefore, InSAR deformation data that correlate positively with rainfall cannot reflect landslide deformation, indicating any correlation with landslide deformation. Based on this practical significance, this paper makes the following numerical treatment:

$$D_f = V_{nor} + |r'| \quad (3)$$

where  $D_f$  is the deformation factor,  $V_{nor}$  is the normalized value of the surface deformation rate and  $r'$  is the correlation coefficient after removing the positive value. According to the previous analysis, when the correlation coefficient  $r$  is negative and its value is closer to  $-1$ , it shows that the positive correlation between the increase of rainfall and the increase of surface deformation is greater, while the positive value of the correlation coefficient show that the two are negatively correlated, which is of no practical significance. Therefore, we remove the positive value in the correlation coefficient as the result of the correlation coefficient with practical significance and take the absolute value to calculate and construct our deformation factor. The value of the deformation factor represents the danger degree of the surface deformation in an area where rainfall is considered. The higher the value of the deformation factor, the more dangerous the deformation area is during rainfall conditions.

The deformation factor can be derived from the above equation, and be graded into four classes according to the actual situation of the study area. The landslide hazard matrix was established (Table 2). Among them, H1–H4 represents the preliminary landslide hazard class (from low to high), and Df1–Df4 represents the deformation factor class (from low to high). And the 1–4 in the table indicate represents the final hazard class (from low to high).

**Table 2.** Landslide hazard evaluation matrix.

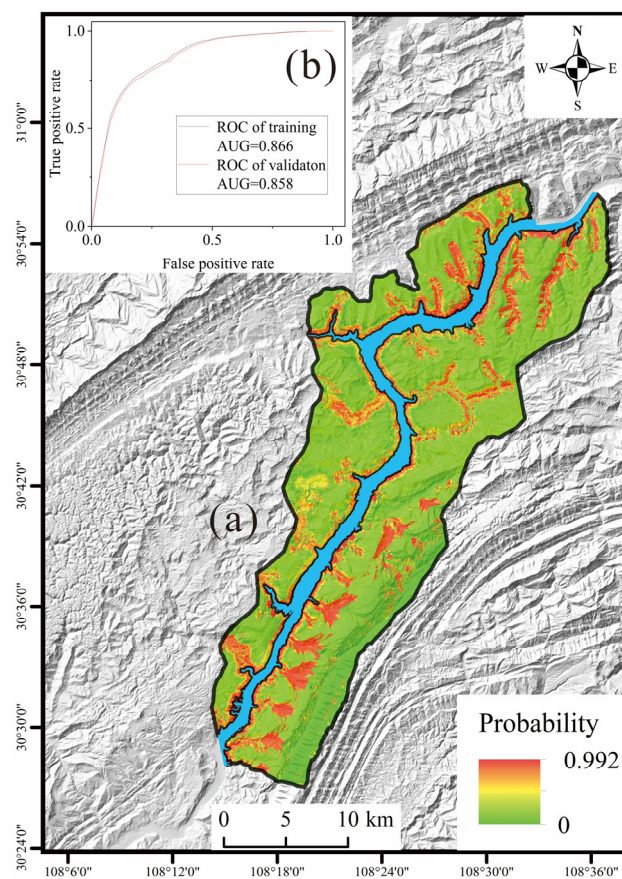
	Df4	Df3	Df2	Df1
H4	4	4	3	2
H3	4	3	2	1
H2	4	3	2	1
H1	4	3	1	1

## 4. Results

### 4.1. Preliminary Landslide Hazard Assessment

#### 4.1.1. Landslide Susceptibility Assessment

Based on the landslide inventory, landslide susceptibility assessment considering 11 evaluation factors was obtained by the SVM method, as shown in Figure 5. The spatial probability for predicting landslide occurrence ranges from 0 to 0.992. The areas where the spatial probability value is greater than 0.8 cover 9.05% of the whole area. Most of these areas are distributed on both sides of the Yangtze River and the gullies. The areas where the spatial probability value is less than 0.2 cover 61.60% of the whole area. Most of them are far away from the Yangtze River. Through the predicted landslide susceptibility map, the distance to the river and the distance to the gully are two major factors in landslide occurrence.

**Figure 5.** (a) Landslide susceptibility map produced by SVM; (b) the ROCs of SVM.

The Receiver Operating Characteristic (ROC) curve and the Area Under the ROC Curve (AUC) are used to evaluate the performance of the training model. The ROC curves of training and validation in this study are shown in Figure 5b. Their corresponding AUC values are 0.866 and 0.858, which are greater than 0.8. The statistical result of the susceptibility is shown in Figure 6. The mean and standard deviation (SD) of the susceptibility results are 0.3093 and 0.2693, respectively. The susceptibility probability is mainly distributed in 0.1–0.2 and 0.8–0.9, and the discrimination is good. These result, including standard

deviation, proves that the trained model has a good performance and also verifies the reliability of landslide susceptibility assessment.

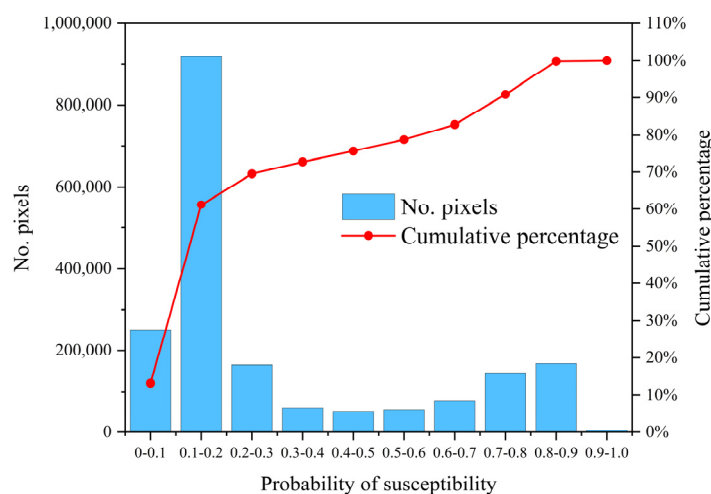


**Figure 6.** Statistic chart of landslide susceptibility probability.

#### 4.1.2. Landslide Hazard Assessment Based on Rainfall

According to the definition of landslide hazard (Equation (1)), the probability of landslide occurrence under certain specific rainfall conditions was selected as the temporal probability of landslide occurrence. The recorded rainfall data from 1997–2017 was statistically analyzed. The 5-day antecedent total rainfall was divided into four levels: 0 mm, 0–50 mm, 50–100 mm and >100 mm (Table 3). During these 20 years, rainfall events of 0–50 mm occurred 5608 times, while rainfall events of 50–100 mm and >100 mm occurred 545 and 85 times, respectively. When the 5-day antecedent total rainfall was less than 50 mm, 108 landslide events occurred in the area, which accounted for 55.96% of the total landslide events. A total of 59 landslide events occurred for the 5-day antecedent total rainfall of 50–100 mm, which accounted for 30.57% of the total landslides. There were 26 landslide events for the 5-day antecedent rainfall of larger than 100 mm. It accounted for 13.47% of the total landslides. The temporal probabilities of landslide occurrence under the four different rainfall conditions are 0, 0.0193, 0.1038 and 0.3059.

According to Equation (1), the landslide hazard under different rainfall conditions was calculated based on the landslide susceptibility analysis and the temporal probability of landslide occurrence. Based on field investigation experience, the landslide hazard index was divided into four categories: H1 (0~0.0085), H2 (0.0085~0.0607), H3 (0.0607~0.0883) and H4 (>0.0883). The larger the landslide hazard index, the higher the landslide hazard zone. The preliminary landslide hazard map was obtained and shown in Figure 7.

**Table 3.** Statistics on rainfall events and landslide occurrence.

	5-day Antecedent Total Rainfall			
	0	0–50	50–100	>100
Rainfall event	1062	5608	545	85
Percentage	14.55%	76.82%	7.47%	1.16%
Landslide event	0	108	59	26
Percentage	0	55.96%	30.57%	13.47%
Time probability	0	0.019258	0.10826	0.30588

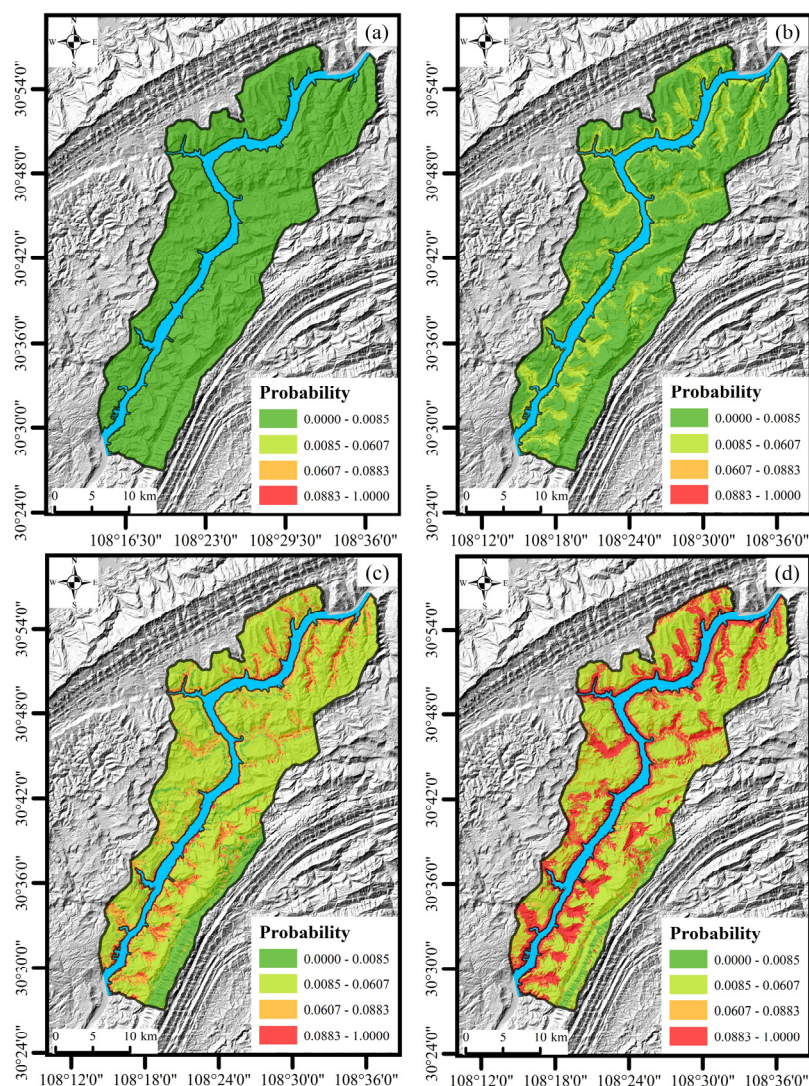


**Figure 7.** Preliminary landslide hazard under different rainfall conditions. (a) Rainfall identity of 0; (b) rainfall identity of 0–50; (c) rainfall identity of 50–100; (d) rainfall identity of larger than 100 mm.

## 4.2. Landslide Hazard Assessment Considering Surface Deformation

### 4.2.1. Surface Deformation and Correlation Analysis

The ground control points were extracted from PS-InSAR and applied in the first inversion of SBAS-InSAR. In order to obtain more comprehensive surface deformation in the area, interferometric image pairs with better interferometric effects and more coherent areas were carefully selected for subsequent processing. The final annual surface deformation velocity is shown in Figure 8. The LOS velocities range from  $-97$  mm/year to  $70$  mm/year. The areas where deformation velocity ranges from  $-10$  mm/year to  $10$  mm/year account for 63.62% of the study area. For the south and northeast areas with inconsistent deformation points, the interpolation method was applied to obtain a comprehensive surface deformation rate in these areas.

In order to analyze the correlation between surface deformation and rainfall, statistical analysis of surface deformation and rainfall within each time unit was conducted. For surface deformation, the difference in surface deformation was obtained between the two images before and after the time unit. For areas without deformation monitoring points, the cumulative surface deformation for that time unit was calculated using ordinary kriging interpolation. Rainfall data were interpolated in the study area based on 12 rainfall monitoring points to obtain the cumulative rainfall distribution in each time unit.

Pearson's correlation coefficient formula (Equation (2)) was used for raster calculations on each pixel. The distribution of correlation coefficients between surface deformation and rainfall was obtained in the study area, and it is shown in Figure 9. In the figure, positive values indicate a positive correlation between rainfall and surface deformation, while negative values indicate a negative correlation. The correlation coefficient ranges from  $-0.2$  to  $0.2$ , which accounts for 68.94% of pixels, indicating a relatively low correlation between surface deformation and rainfall in most areas.

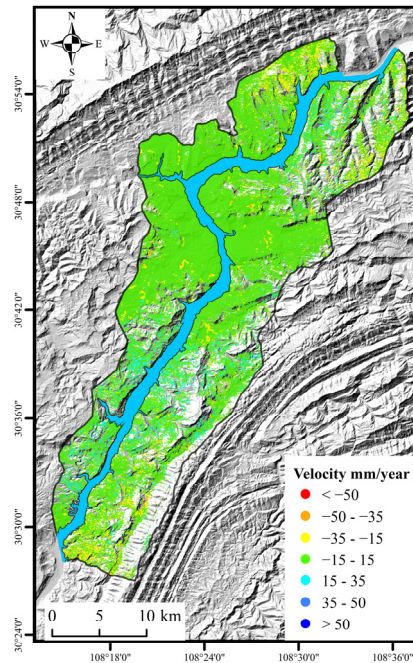


Figure 8. Annual mean rate of surface deformation.

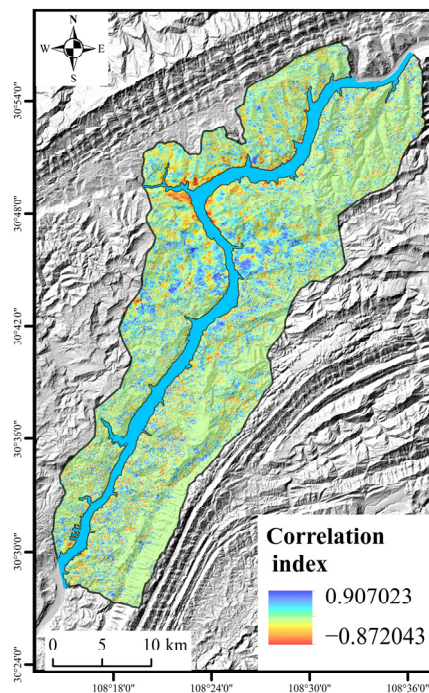


Figure 9. Distribution of correlation coefficient between surface deformation and rainfall.

#### 4.2.2. Landslide Hazard Assessment Considering Surface Deformation

According to the landslide hazard assessment method described above (Equation (3)), the annual surface deformation rate and the processed correlation coefficient are normalized. They are equivalently summed to obtain the final deformation factor map (Figure 10). The deformation factors were divided into four levels: very low-Df1 (0~0.1), low-Df2 (0.1~0.3), moderate-Df3 (0.3~0.6) and high-Df4 (>0.6). Based on the proposed landslide hazard assessment matrix, the final landslide hazard map was obtained considering surface deformation and rainfall, which is shown in Figure 11.

Figure 12 presented statistical results on the preliminary and final landslide hazard. There is a close relationship between rainfall intensity and landslide hazard degree. With increasing rainfall, the areas with low hazards decrease while those with high hazards increase. In the preliminary landslide hazard assessment, 31.05% of pixels were at a high hazard level when the 5-day antecedent total rainfall exceeded 100 mm, while only 4.11% of pixels were at a very low hazard level. However, no area was at a high hazard level when the 5-day antecedent total rainfall was less than 50 mm.

The same characteristic was exhibited in the final landslide hazard assessment considering the deformation factor. When the 5-day antecedent total rainfall was less than 50 mm, only 6.41% of the areas were at a moderate risk level or above. When the 5-day antecedent total rainfall exceeded 100 mm, the proportion of areas at a moderate hazard level or above was 15.98%. At the same rainfall intensity, the proportion of areas at a high or moderate hazard level in the final landslide hazard assessment was smaller than in the preliminary hazard assessment. In the preliminary landslide hazard result, the proportion of pixels with high landslide hazard levels was 0%, 0%, 6.61% and 31.05% under four different rainfall conditions. In the final landslide hazard result, the proportion of pixels with high hazard levels was 0.44%, 0.44%, 1.13% and 2.78%. For rainfall intensity of larger than 100 mm, the proportion with a high hazard level in the final hazard result was significantly lower than that in the preliminary landslide hazard. After considering the surface deformation, the overall hazard in the area was relatively low.

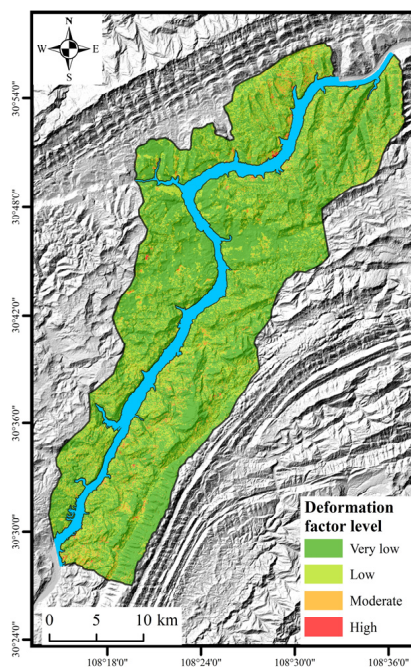
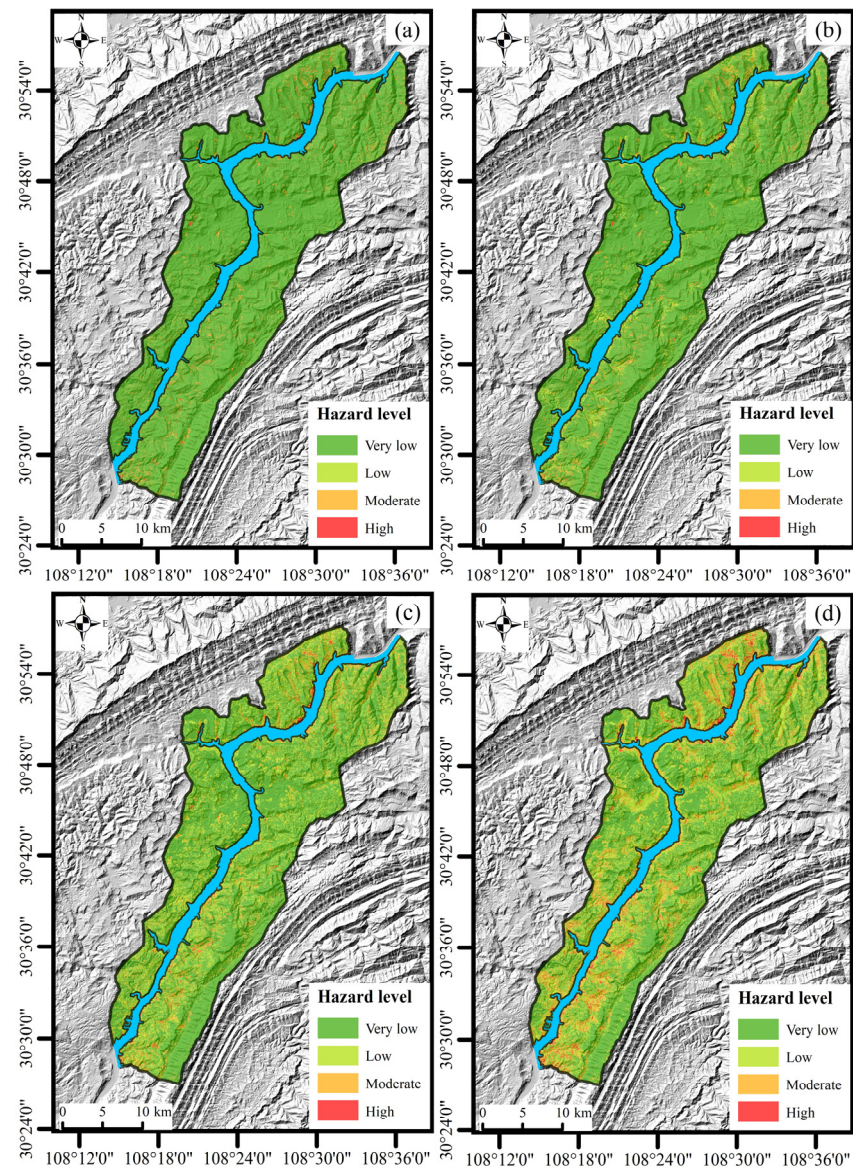
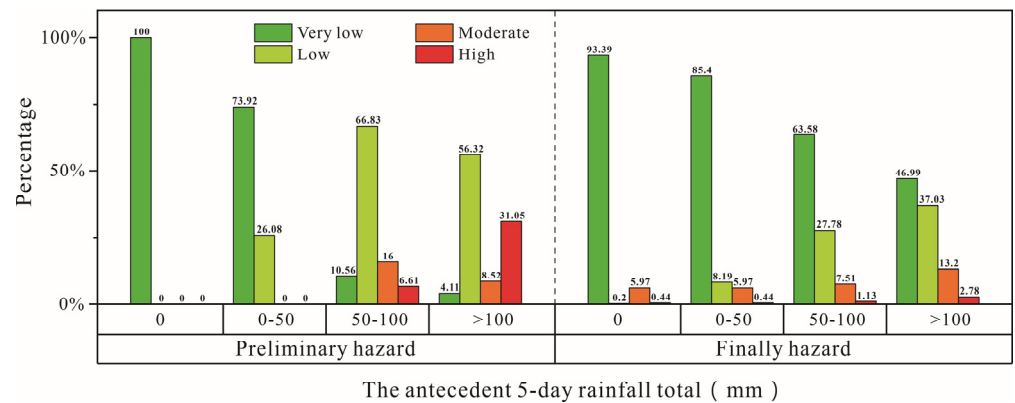


Figure 10. Deformation factor map.



**Figure 11.** Final landslide hazard map for different rainfall conditions. (a) Rainfall intensity of 0; (b) rainfall intensity of 0–50; (c) rainfall intensity of 50–100; (d) rainfall intensity of larger than 100 mm.



**Figure 12.** Landslide hazard results statistics for different rainfall conditions.

## 5. Discussions

Based on time-series InSAR technology, the surface deformation information in the area was obtained during the specific time period. These deformations not only reflect slope deformations caused by rainfall but also those caused by other triggering factors such as reservoir water fluctuation. When directly applying the surface deformation to landslide hazard assessment, these ‘non-landslide’ deformations may result in a mis-assessment, which leads to ‘false positives’ and ‘false negatives’ errors [28]. For example, it may overestimate the hazard of non-landslide deformation areas or underestimate the hazard of slow-moving landslides with less obvious deformation features, both of which can impact landslide hazard assessment results.

For small rainfall intensity, the overall landslide hazard in the preliminary hazard assessment was low, and the proportion of pixels with medium and high landslide hazard levels were both 0. However, there were still some areas with medium or high hazard levels in the final landslide hazard assessment. The number of landslides was counted at different landslide hazard levels, shown in Figure 13. In the preliminary landslide hazard assessment (Figure 13a), the landslide hazard levels undergo drastic changes with the increase in rainfall intensity. When the 5-day antecedent rainfall total was 0, the hazard level of all landslides was very low. When the 5-day antecedent total rainfall would exceed 100mm, the majority of landslides had a high hazard level. In the final landslide hazard assessment (Figure 13b), the number of landslides with the increase in rainfall intensity shows a gradual growth trend at low, moderate and high hazard levels.

Figure 14 illustrates the proportion of landslide pixels to the hazard pixels in the study region at different landslide hazard levels. In the preliminary landslide hazard level, the overall proportion is relatively low, and with cases of extreme fluctuations, the hazard assessment result was not stable enough. In the final landslide hazard level, the proportion shows the characteristics of stable low-hazard proportions and high-hazard proportions, except that the proportion of high is reduced when the 5-day antecedent rainfall total was 100 mm. This implies that the final landslide hazard assessment result was relatively stable, and the accuracy of assessing high landslide hazard areas was also higher. For small rainfall intensity, the final landslide hazard result considered those locations with significant deformation to have a certain level of hazard due to external factors. For larger rainfall intensity, the overall landslide hazard level in the final landslide hazard assessment was a noticeable decrease. However, some visibly deformed high-hazard areas were not overlooked. This indicates that incorporating the deformation factor can effectively adjust the landslide hazard based on the existing deformation.

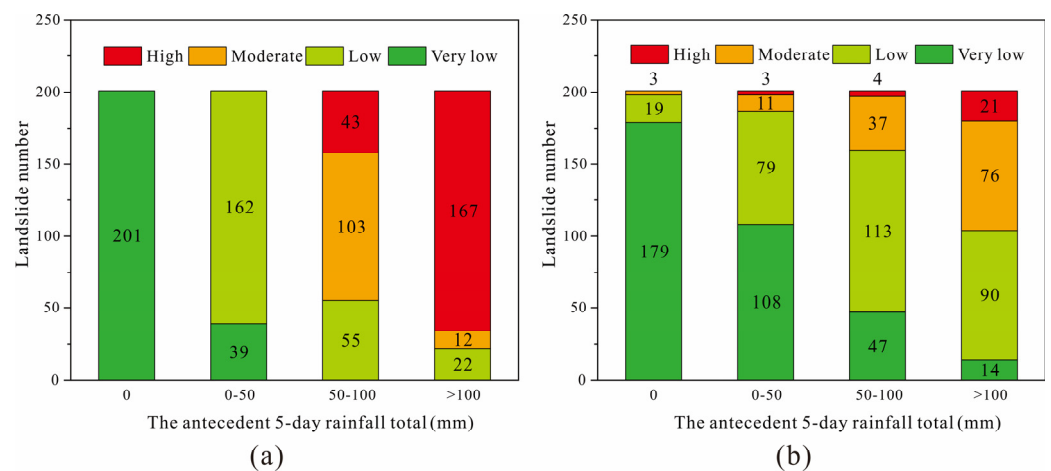


**Figure 13.** Number of landslides at different landslide hazard levels. (a) Preliminary landslide hazard result; (b) final landslide hazard result.

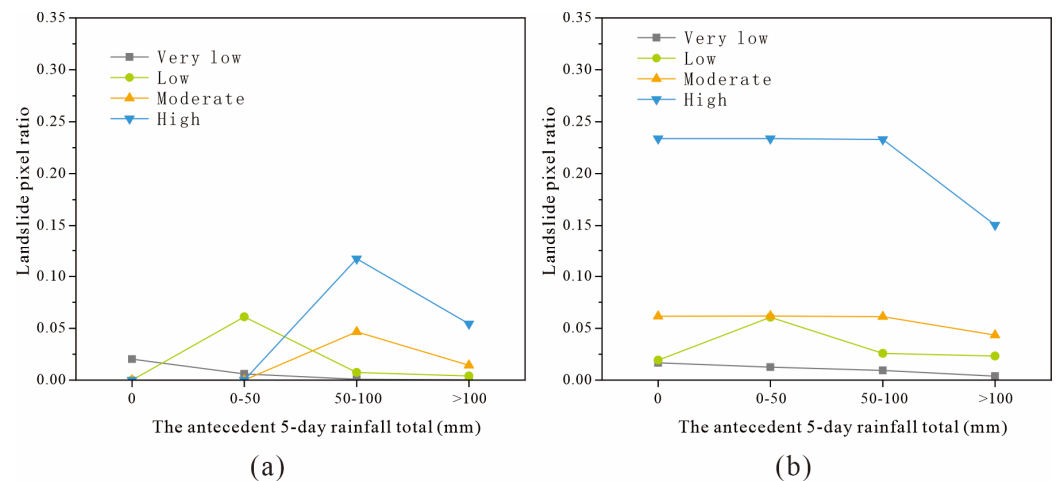


**Figure 14.** Proportion of landslide pixels to hazard pixels at different landslide hazard levels. (a) preliminary landslide hazard result; (b) final landslide hazard result.

In order to further validate the effectiveness of this method, a step-by-step comparative analysis combining preliminary landslide hazard, surface deformation, correlation coefficient, deformation factor and final landslide hazard was performed for the 5-day antecedent total rainfall exceeding 100 mm. Several regions with significant evaluation characteristics were identified in the process, as shown in Figure 15. In Figure 15a, the deformation at this location was caused by slope excavation near the airport, and the deformation was not directly related to rainfall through correlation analysis. The deformation factor indicated that the main deformation impact zone was near the excavated slope. Although the preliminary landslide hazard was relatively low, the landslide hazard ultimately increased near the excavation site after considering the slope excavation. In Figure 15b, there was a large number of deformation areas near the reservoir bank due to a construction project, but correlation analysis indicated that these deformations were not directly related to rainfall. There was an initial high hazard level in the preliminary landslide hazard assessment. However, the moderate landslide hazard result was obtained due to these deformations caused by human engineering activities. If the hazard of the area was evaluated directly on the basis of the surface deformation without a correlation analysis, the area might be considered to have the highest level of hazard. In Figure 15c, the overall surface deformation in the landslide area was relatively small. However, the correlation analysis revealed a close relationship between the surface deformation at certain locations and rainfall. The final result aligned with the current deformation state of the landslide's hazard. If the hazard of the area was evaluated only by the surface deformation, those locations where the surface deformation varies significantly with rainfall might be neglected, thus obtaining a lower hazard, which is very unreasonable. In Figure 15d, significant surface deformation was observed in the landslide. Deformation related to rainfall is mainly concentrated in specific locations at the trailing edge and the leading edge of the landslide. This indicated that other larger deformations may be caused by human activities such as land cultivation, which resulted in a more precise distribution of landslide hazards.

By utilizing the correlation analysis between rainfall and surface deformation to construct the deformation factor, effective surface deformation information could be identified, especially in cases where landslides were triggered by rainfall or human engineering activities. The method for landslide hazard assessment could establish the direct correction with the preliminary landslide hazard and avoid errors caused by InSAR anomalies. The landslide hazard assessment result was closer to that of the deformation areas of slopes and landslides. The areas with minor deformation but significantly influenced by rainfall were not neglected. Compared to the general method of hazard assessment in conjunction with surface deformation, the areas with large surface deformation or high landslide preliminary

hazard but unrelated to rainfall-induced landslide deformation were not overestimated. Therefore, this method would enhance the efficiency of landslide hazard assessment.

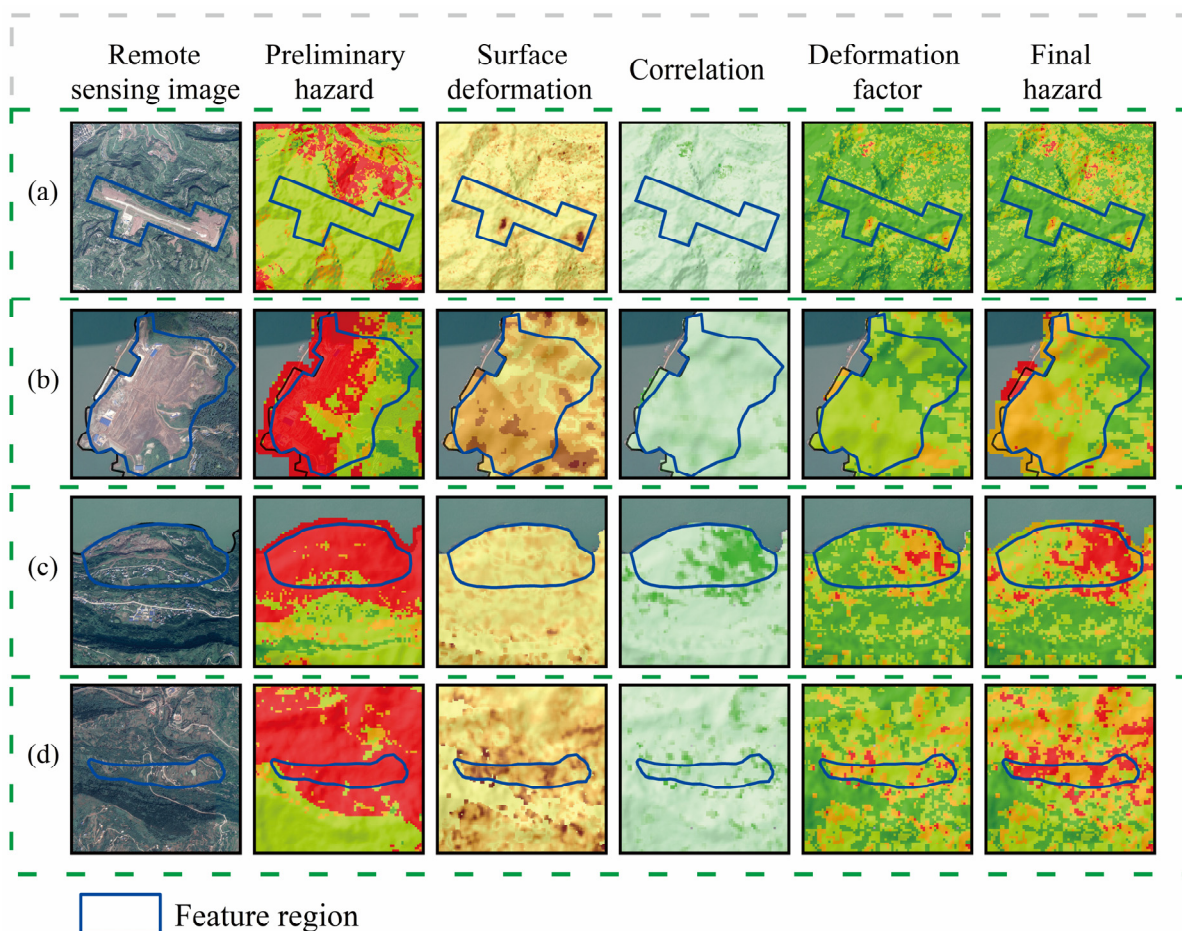


**Figure 15.** Comparison of preliminary hazard, surface deformation and final landslide hazard. The (a–d) represent four different typical regions.

## 6. Conclusions

In order to obtain more accurate landslide hazard assessment results, the correlation analysis of rainfall and surface deformation was applied to the landslide hazard assessment based on time series InSAR and landslide spatial-temporal probability. The research results indicate that (i) the regional landslide hazard level increases with the intensity of rainfall in preliminary hazard assessment. When the antecedent 5-day rainfall total exceeds 100 mm, 31.05% of the area is classified as a high landslide hazard subarea, while only 4.11% of the area is classified as a very low landslide hazard subarea. (ii) The final landslide hazard assessment result constructed by preliminary hazard and the deformation factor effectively adjusts and corrects the existing hazard levels in some subarea. When the antecedent 5-day rainfall total is less than 50 mm, the hazard level for 6.41% of the areas is moderate or higher. When the antecedent 5-day rainfall total exceeds 100 mm, the hazard level for 15.98% of the areas is moderate or higher, with a high-risk proportion of 2.78%. Overall, the distribution of landslide hazards is more reasonable.

As discussed above, it is possible to accurately determine the landslide hazard level, effectively eliminating potential bias in landslide hazard assessment by introducing the deformation factor obtained through the correlation analysis between the surface deformation and rainfall. Compared with general hazard assessment, this method can effectively characterize the current state of deformation and potential hazard state of landslides and slopes, and this method can reduce the hazard misclassification due to landslide informa-

tion caused by different triggers of surface deformation, thus determining the landslide hazard class more accurately. The landslide hazard assessment method proposed in this study significantly enhances the reliability of hazard assessments, especially in areas where the time-series InSAR method is available and applicable. In the future, it is necessary to delve into the various influencing factors of landslides and the periodic characteristics of these factors to achieve more precise dynamic hazard assessments.

**Author Contributions:** X.S. processed the dataset, carried out the analysis, and wrote the original draft of this manuscript. W.Z. helped process and analyze some of the data. X.X., S.Y. and Y.S. provided full guidance on experimental processing and manuscript writing. D.L. revised and improved this manuscript. All authors contributed to the study's conception and design. All authors have read and agreed to the published version of the manuscript.

**Funding:** This research was funded by the project “Geological Disasters Quantitative Hazard Prediction and Dynamic Risk Evaluation of on Random Slopes” (grant no. 2023YFC3007203), which is financed by National Key Research and Development Program of China.

**Data Availability Statement:** The Sentinel-1A images and precise orbit data were provided by the European Space Agency. Data such as rainfall and landslides are provided by the project that supported this article. If readers want to have the data, they can request it by e-mail from the authors.

**Acknowledgments:** We thank Jingxue Chen for her help in mapping. We thank Bingbing Ni for providing valuable suggestions in writing this article.

**Conflicts of Interest:** The authors declare that they have no known competing financial interests or personal relationships that could have appeared to influence the work reported in this paper.

## References

- Petley, D.N.; Hearn, G.J.; Hart, A.; Rosser, N.J.; Dunning, S.A.; Oven, K.; Mitchell, W.A. Trends in landslide occurrence in Nepal. *Nat. Hazards* **2007**, *43*, 23–44. [[CrossRef](#)]
- Fan, X.; Scaringi, G.; Korup, O.; West, A.J.; Van Westen, C.J.; Tanyas, H.; Hovius, N.; Hales, T.C.; Jibson, R.W.; Allstadt, K.E.; et al. Earthquake-induced chains of geologic hazards: Patterns, mechanisms, and impacts. *Rev. Geophys.* **2019**, *57*, 421–503. [[CrossRef](#)]
- Segoni, S.; Piciullo, L.; Gariano, S.L. A review of the recent literature on rainfall thresholds for landslide occurrence. *Landslides* **2018**, *15*, 1483–1501. [[CrossRef](#)]
- Fell, R.; Corominas, J.; Bonnard, C.; Cascini, L.; Leroi, E.; Savage, W. Guidelines for landslide susceptibility, hazard and risk zoning for land use planning. *Eng. Geol.* **2008**, *102*, 85–98. [[CrossRef](#)]
- Constantin, M.; Bednarik, M.; Jurchescu, M.C.; Vlaicu, M. Landslide susceptibility assessment using the bivariate statistical analysis and the index of entropy in the Sibiciu Basin (Romania). *Environ. Earth Sci.* **2011**, *63*, 397–406. [[CrossRef](#)]
- Esposito, C.; Mastrantonio, G.; Marmoni, G.M.; Antonielli, B.; Caprari, P.; Pica, A.; Schilirò, L.; Mazzanti, P.; Bozzano, F. From theory to practice: Optimisation of available information for landslide hazard assessment in Rome relying on official, fragmented data sources. *Landslides* **2023**, *20*, 2055–2073. [[CrossRef](#)]
- Reichenbach, P.; Rossi, M.; Malamud, B.; Mihir, M.; Guzzetti, F. A review of statistically based landslide susceptibility models. *Earth-Sci. Rev.* **2018**, *180*, 60–91. [[CrossRef](#)]
- Carrión-Mero, P.; Montalván-Burbano, N.; Morante-Carballo, F.; Quesada-Román, A.; Apolo-Masache, B. Worldwide research trends in landslide science. *Int. J. Environ. Res. Public Health* **2021**, *18*, 9445. [[CrossRef](#)] [[PubMed](#)]
- Torizin, J.; Wang, L.; Fuchs, M.; Tong, B.; Balzer, D.; Wan, L.; Kuhn, D.; Li, A.; Chen, L. Statistical landslide susceptibility assessment in a dynamic environment: A case study for Lanzhou City, Gansu Province, NW China. *J. Mt. Sci.* **2018**, *15*, 1299–1318. [[CrossRef](#)]
- Nefeslioglu, H.A.; Gorum, T. The use of landslide hazard maps to determine mitigation priorities in a dam reservoir and its protection area. *Land Use Policy* **2020**, *91*, 104363. [[CrossRef](#)]
- Preuth, T.; Glade, T.; Demoulin, A. Stability analysis of a human-influenced landslides in eastern Belgium. *Geomorphology* **2010**, *120*, 38–47. [[CrossRef](#)]
- Guzzetti, F.; Reichenbach, P.; Cardinali, M.; Galli, M.; Ardizzone, F. Probabilistic landslide hazard assessment at the basin scale. *Geomorphology* **2005**, *72*, 272–299. [[CrossRef](#)]
- Kovrov, O.; Kolesnyk, V.; Buchavyi, Y. Development of the landslide risk classification for natural and man-made slopes based on soil watering and deformation extent. *Min. Miner. Depos.* **2020**, *14*, 105–112. [[CrossRef](#)]
- Kontoes, C.; Loupasakis, C.; Papoutsis, I.; Alatza, S.; Poyiadji, E.; Ganas, A.; Psychogyiou, C.; Kaskara, M.; Antoniadi, S.; Spanou, N. Landslide susceptibility mapping of central and Western Greece, combining NGI and WoE methods, with remote sensing and ground truth data. *Land* **2021**, *10*, 402. [[CrossRef](#)]
- Ciampalini, A.; Raspini, F.; Lagomarsino, D.; Catani, F.; Casagli, N. Landslide susceptibility map refinement using PSInSAR data. *Remote Sens. Environ.* **2016**, *184*, 302–315. [[CrossRef](#)]

16. Zhang, Y.; Chen, Y.; Ming, D.; Zhu, Y.; Ling, X.; Zhang, X.; Lian, X. Landslide hazard analysis based on SBAS-InSAR and MCE-CNN model: A case study of Kongtong, Pingliang. *Geocarto Int.* **2022**, *38*, 1–22. [[CrossRef](#)]
17. Ferretti, A.; Prati, C.; Rocca, F. Permanent scatterers in SAR interferometry. *IEEE Trans. Geosci. Remote Sens.* **2001**, *39*, 8–20. [[CrossRef](#)]
18. Akbarimehr, M.; Motagh, M.; Haghshenas-Haghighi, M. Slope stability assessment of the Sarcheshmeh landslide, Northeast Iran, investigated using InSAR and GPS observations. *Remote Sens.* **2013**, *5*, 3681–3700. [[CrossRef](#)]
19. Intrieri, E.; Raspini, F.; Fumagalli, A.; Lu, P.; Del Conte, S.; Farina, P.; Allievi, J.; Ferretti, A.; Casagli, N. The Maoxian landslide as seen from space: Detecting precursors of failure with Sentinel-1 data. *Landslides* **2018**, *15*, 123–133. [[CrossRef](#)]
20. Zhang, Y.; Meng, X.; Jordan, C.; Novellino, A.; Dijkstra, T.; Chen, G. Investigating slow-moving landslides in the Zhouqu region of China using InSAR time series. *Landslides* **2018**, *15*, 1299–1315. [[CrossRef](#)]
21. Yang, S.; Li, D.; Liu, Y.; Xu, Z.; Sun, Y.; She, X. Landslide Identification in Human-Modified Alpine and Canyon Area of the Niulan River Basin Based on SBAS-InSAR and Optical Images. *Remote Sens.* **2023**, *15*, 1998. [[CrossRef](#)]
22. Urgilez Vinueza, A.; Handwerger, A.L.; Bakker, M.; Bogaard, T. A new method to detect changes in displacement rates of slow-moving landslides using InSAR time series. *Landslides* **2022**, *19*, 2233–2247. [[CrossRef](#)]
23. Novellino, A.; Cesarano, M.; Cappelletti, P.; Di Martire, D.; Di Napoli, M.; Ramondini, M.; Sowter, A.; Calcaterra, D. Slow-moving landslide risk assessment combining machine learning and InSAR techniques. *Catena* **2021**, *203*, 105317. [[CrossRef](#)]
24. Zheng, X.; He, G.; Wang, S.; Wang, Y.; Wang, G.; Yang, Z.; Yu, J.; Wang, N. Comparison of machine learning methods for potential active landslide hazards identification with multi-source data. *ISPRS Int. J. Geo Inf.* **2021**, *10*, 253. [[CrossRef](#)]
25. Zhang, G.; Wang, S.; Chen, Z.; Liu, Y.; Xu, Z.; Zhao, R. Landslide susceptibility evaluation integrating weight of evidence model and InSAR results, west of Hubei Province, China. *Egypt. J. Remote Sens. Space Sci.* **2023**, *26*, 95–106. [[CrossRef](#)]
26. Shan, Y.; Xu, Z.; Zhou, S.; Lu, H.; Yu, W.; Li, Z.; Cao, X.; Li, P.; Li, W. Landslide Hazard Assessment Combined with InSAR Deformation: A Case Study in the Zagunao River Basin, Sichuan Province, Southwestern China. *Remote Sens.* **2024**, *16*, 99. [[CrossRef](#)]
27. Zhou, C.; Cao, Y.; Hu, X.; Yin, K.; Wang, Y.; Catani, F. Enhanced dynamic landslide hazard mapping using MT-InSAR method in the Three Gorges Reservoir Area. *Landslides* **2022**, *19*, 1585–1597. [[CrossRef](#)]
28. Dai, C.; Li, W.; Lu, H.; Zhang, S. Landslide Hazard Assessment Method Considering the Deformation Factor: A Case Study of Zhouqu, Gansu Province, Northwest China. *Remote Sens.* **2023**, *15*, 596. [[CrossRef](#)]
29. Zhang, X.; Chen, L.; Zhou, C. Deformation Monitoring and Trend Analysis of Reservoir Bank Landslides by Combining Time-Series InSAR and Hurst Index. *Remote Sens.* **2023**, *15*, 619. [[CrossRef](#)]
30. Miao, F.; Wu, Y.; Xie, Y.; Li, Y. Prediction of Landslide Displacement with Step-like Behavior Based on Multialgorithm Optimization and a Support Vector Regression Model. *Landslides* **2018**, *15*, 475–488. [[CrossRef](#)]
31. Guzzetti, F.; Reichenbach, P.; Ardizzone, F.; Cardinali, M.; Galli, M. Estimating the quality of landslide susceptibility models. *Geomorphology* **2006**, *81*, 166–184. [[CrossRef](#)]
32. Marjanović, M.; Kovačević, M.; Bajat, B.; Voženilek, V. Landslide susceptibility assessment using SVM machine learning algorithm. *Eng. Geol.* **2011**, *123*, 225–234. [[CrossRef](#)]
33. Dou, J.; Yunus, A.P.; Bui, D.T.; Merghadi, A.; Sahana, M.; Zhu, Z.; Chen, C.W.; Han, Z.; Pham, B.T. Improved landslide assessment using support vector machine with bagging, boosting, and stacking ensemble machine learning framework in a mountainous watershed, Japan. *Landslides* **2020**, *17*, 641–658. [[CrossRef](#)]
34. Bordoni, M.; Vivaldi, V.; Lucchelli, L.; Ciabatta, L.; Brocca, L.; Galve, J.P.; Meisina, C. Development of a data-driven model for spatial and temporal shallow landslide probability of occurrence at catchment scale. *Landslides* **2021**, *18*, 1209–1229. [[CrossRef](#)]
35. Corominas, J.; van Westen, C.; Frattini, P.; Cascini, L.; Malet, J.P.; Fotopoulou, S.; Catani, F.; Van Den Eeckhaut, M.; Mavrouli, O.; Agliardi, F.; et al. Recommendations for the quantitative analysis of landslide risk. *Bull. Eng. Geol. Env.* **2014**, *73*, 209–263. [[CrossRef](#)]
36. Lee, J.H.; Kim, H.; Park, H.J.; Heo, J.H. Temporal prediction modeling for rainfall-induced shallow landslide hazards using extreme value distribution. *Landslides* **2021**, *18*, 321–338. [[CrossRef](#)]
37. Liu, C. *Landslide Risk Assessment at Wanzhou Urban Area in the Three Gorges Reservoir*; China University of Geosciences Press: Wuhan, China, 2014.
38. Del Soldato, M.; Riquelme, A.; Bianchini, S.; Tomàs, R.; Di Martire, D.; De Vita, P.; Moretti, S.; Calcaterra, D. Multisource Data Integration to Investigate One Century of Evolution for the Agnone Landslide (Molise, Southern Italy). *Landslides* **2018**, *15*, 2113–2128. [[CrossRef](#)]
39. Wasowski, J.; Pisano, L. Long-Term InSAR, Borehole Incliner, and Rainfall Records Provide Insight into the Mechanism and Activity Patterns of an Extremely Slow Urbanized Landslide. *Landslides* **2020**, *17*, 445–457. [[CrossRef](#)]
40. Lu, P.; Catani, F.; Tofani, V.; Casagli, N. Quantitative Hazard and Risk Assessment for Slow-Moving Landslides from Persistent Scatterer Interferometry. *Landslides* **2014**, *11*, 685–696. [[CrossRef](#)]
41. Ferretti, A.; Prati, C.; Rocca, F. Nonlinear subsidence rate estimation using permanent scatterers in differential SAR interferometry. *IEEE Trans. Geosci. Remote Sens.* **2000**, *38*, 2202–2212. [[CrossRef](#)]
42. Berardino, P.; Fornaro, G.; Lanari, R.; Sansosti, E. A new algorithm for surface deformation monitoring based on small baseline differential SAR interferograms. *IEEE Trans. Geosci. Remote Sens.* **2002**, *40*, 2375–2383. [[CrossRef](#)]
43. Zhang, J.; Gong, Y.; Huang, W.; Wang, X.; Ke, Z.; Liu, Y.; Huo, A.; Adnan, A.; Abuarab, M.E.-S. Identification of Potential Landslide Hazards Using Time-Series InSAR in Xiji County, Ningxia. *Water* **2023**, *15*, 300. [[CrossRef](#)]

44. Wang, J.; Xiao, L.; Zhang, J.; Zhu, Y. Deformation characteristics and failure mechanisms of a rainfall-induced complex landslide in Wanzhou County, Three Gorges Reservoir, China. *Landslides* **2020**, *17*, 419–431. [[CrossRef](#)]
45. Buytaert, W.; Celleri, R.; Willems, P.; De Bievre, B.; Wyseure, G. Spatial and temporal rainfall variability in mountainous areas: A case study from the south Ecuadorian Andes. *J. Hydrol.* **2006**, *329*, 413–421. [[CrossRef](#)]
46. Singh, N.; Maddheshiya, S.K.; Jha, M.; Tignath, S.; Singh, B.N. Hydrogeomorphic assessment of badlands in part of the Mandakini River watershed, Chitrakoot, India. *Arab. J. Geosci.* **2020**, *13*, 1066. [[CrossRef](#)]
47. Dong, J.; Niu, R.; Li, B.; Xu, H.; Wang, S. Potential landslides identification based on temporal and spatial filtering of SBAS-InSAR results. *Geomat. Nat. Hazards Risk* **2023**, *14*, 52–75. [[CrossRef](#)]

**Disclaimer/Publisher’s Note:** The statements, opinions and data contained in all publications are solely those of the individual author(s) and contributor(s) and not of MDPI and/or the editor(s). MDPI and/or the editor(s) disclaim responsibility for any injury to people or property resulting from any ideas, methods, instructions or products referred to in the content.